J|A|C|S COMMUNICATIONS

Published on Web 06/29/2010

Rapid Acquisition of Multidimensional Solid-State NMR Spectra of Proteins Facilitated by Covalently Bound Paramagnetic Tags

Philippe S. Nadaud, Jonathan J. Helmus, Ishita Sengupta, and Christopher P. Jaroniec*

Department of Chemistry, The Ohio State University, Columbus, Ohio 43210

Received April 26, 2010; E-mail: jaroniec@chemistry.ohio-state.edu

Abstract: We describe a condensed data collection approach that facilitates rapid acquisition of multidimensional magic-angle spinning solid-state nuclear magnetic resonance (SSNMR) spectra of proteins by combining rapid sample spinning, optimized low-power radio frequency pulse schemes and covalently attached paramagnetic tags to enhance protein ^{1}H spin−lattice relaxation. Using EDTA-Cu^{2+}-modified K28C and N8C mutants of the B1 immunoglobulin binding domain of protein G as models, we demonstrate that high resolution and sensitivity 2D and 3D SSNMR chemical shift correlation spectra can be recorded in as little as several minutes and several hours, respectively, for samples containing ∼0.1−0.2 μmol of ^{13}C,^{15}N- or ^{2}H,^{13}C,^{15}N-labeled protein. This mode of data acquisition is naturally suited toward the structural SSNMR studies of paramagnetic proteins, for which the typical ^{1}H longitudinal relaxation time constants are inherently a factor of at least ∼3−4 lower relative to their diamagnetic counterparts. To illustrate this, we demonstrate the rapid site-specific determination of backbone amide ^{15}N longitudinal paramagnetic relaxation enhancements using a pseudo-3D SSNMR experiment based on ^{15}N−^{13}C correlation spectroscopy, and we show that such measurements yield valuable long-range ^{15}N−Cu^{2+} distance restraints which report on the three-dimensional protein fold.

Solid-state nuclear magnetic resonance (SSNMR) has recently emerged as a unique spectroscopic method, capable of providing atomic-resolution images of biological macromolecules that are not amenable to analysis by other high-resolution techniques.[1] It is well-known, however, that conventional SSNMR experiments employing moderate magic-angle spinning (MAS) rates (∼10−25 kHz) and high radio frequency (RF) ^{1}H decoupling fields generally suffer from inherently low sensitivity. This stems, in part, from the fact that most of the total experiment time is occupied by ∼2−3 s recycle delays between successive scans, required to restore the equilibrium ^{1}H magnetization for cross-polarization[2] and minimize RF sample heating and probe duty cycle. One general approach toward reducing interscan delays and enhancing the sensitivity of SSNMR experiments involves the introduction of paramagnetic species into the sample of interest.[3] Such paramagnetic dopants promote rapid longitudinal relaxation of the nearby ^{1}H spins and this effect is transferred to other protons via efficient ^{1}H−^{1}H spin diffusion,[4] the end result being that all ^{1}H nuclei return to equilibrium with an effective longitudinal relaxation time constant (T_1), which is considerably less than that for an undoped diamagnetic sample.

Recently, Ishii and co-workers have introduced a paramagnetic relaxation-assisted condensed data collection (PACC) method for increasing the sensitivity of SSNMR spectra of biomolecules,[5] which combines paramagnetic doping,[3] rapid MAS ($\nu_r \geq$ ∼40 kHz) and low-power RF pulse schemes,[6] and short recycle delays (∼0.2−0.3 s). This approach considerably accelerates SSNMR data acquisition and has enabled the analysis of nanomolar quantities of ^{13}C,^{15}N-labeled proteins. The paramagnetic dopant in this case is an aqueous Cu(II)-EDTA (or Ni(II)-EDTA) complex, diffused into a hydrated protein SSNMR sample, and the proposed ^{1}H T_1 relaxation enhancement mechanism involves Cu(II)-EDTA in the solution phase making transient contacts with protein molecules immobilized in microcrystals or other ordered assemblies. These transient contacts lead to rapid relaxation by Cu^{2+} ions of the protein ^{1}H nuclei at the solid−liquid interface, followed by spin diffusion to equalize the ^{1}H longitudinal relaxation rates throughout the immobilized protein sample.[5] The PACC approach has been extended to studies of highly deuterated proteins,[7] and analogous fast recycling SSNMR experiments have been reported for native metalloproteins.[8] The use of Cu(II)-chelating lipids to enhance the sensitivity of SSNMR spectra of membrane-associated peptides has also been demonstrated very recently.[9]

We have recently shown that long-range, up to ∼20 Å, electron−nucleus distance restraints can be obtained using MAS SSNMR techniques in ^{13}C,^{15}N-labeled proteins modified with covalently attached paramagnetic tags, including nitroxide spin labels[10] and transition metal−EDTA complexes.[11] Here we show that such proteins, which inherently display ∼3−4-fold reduced ^{1}H T_1 times relative to their diamagnetic counterparts, are ideally suited for application of PACC-type condensed data acquisition schemes and permit high resolution and sensitivity 2D and 3D SSNMR spectra to be recorded within several minutes to several hours for samples containing ∼0.1−0.2 μmol of labeled protein. Most importantly, this accelerated mode of data collection enables the rapid determination of site-specific nuclear paramagnetic relaxation enhancements (PREs), which yield valuable long-range information about the three-dimensional protein fold.

The experiments are demonstrated on EDTA-Cu^{2+}-modified N8C and K28C mutants of the B1 immunoglobulin binding domain of protein G (GB1), referred to as 8EDTA-Cu^{2+} and 28EDTA-Cu^{2+} for brevity, but note that similar data were obtained for four other EDTA-Cu^{2+} GB1 variants. Protein microcrystals for SSNMR were prepared by precipitating ∼1 mg (∼150 nmol) of ^{13}C,^{15}N (CN) or ^{2}H,^{13}C,^{15}N (DCN) labeled EDTA-Cu^{2+} proteins with unlabeled wild-type GB1 in an ∼1:3 molar ratio[11] (see Supporting Information). At 40 kHz MAS, the ^{1}H T_1 times of CN- and DCN-EDTA-Cu^{2+} proteins were determined by standard inversion−recovery methods to be ∼120 ms (data not shown), while the ^{1}H T_1's of corresponding diamagnetic EDTA-Zn^{2+} samples were ∼450 ms.

In Figure 1 we show representative 2D and 3D chemical shift correlation spectra of DCN-28EDTA-Cu^{2+} acquired at 40 kHz MAS using optimized low-power pulse schemes (Figures S1 and S2). The 2D NCO spectrum (Figure 1A), which was recorded in only ∼7 min (note that this could be reduced further with only a modest decrease in sensitivity or, alternatively, slightly higher sensitivity could be achieved within the same experiment time by using shorter recycle delays, ∼1.2−1.5 × instead of 3 × ^{1}H T_1), exhibits particularly high digital resolution due to the use of a spin-state selective (S^3E) filter to suppress ^{13}CO−^{13}Cα J-couplings during detection[12] and relatively long evolution times in t_1 and t_2. We note here that signals arising from all backbone amide ^{15}N's, including residues in the vicinity of the paramagnetic center (located ∼10 Å away from the Cu^{2+} ion[11]), are readily detected in this spectrum; the cross-peak signal-to-noise (S/N)

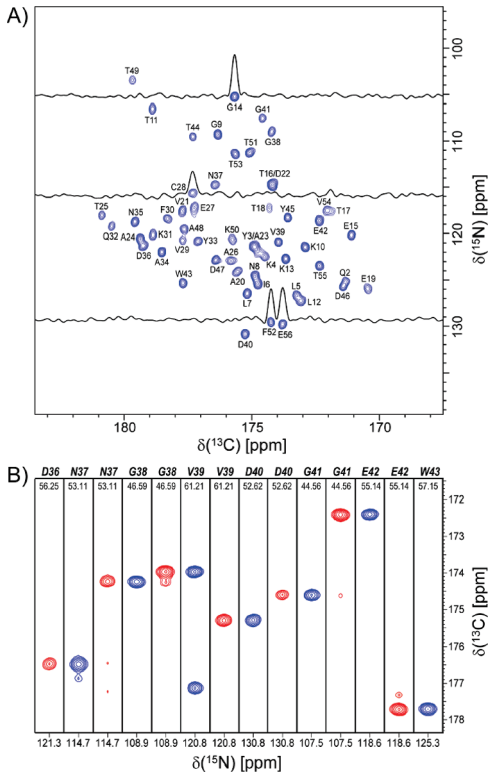

Figure 1. Solid-state NMR spectra of $^{2}H,^{13}C,^{15}N$-labeled 28EDTA-Cu^{2+} (~150 nmol protein) back-exchanged with H_2O, recorded at 11.7 T and 40 kHz MAS. (A) 2D $^{15}N-^{13}CO$ (NCO) spectrum recorded using the 2D NCO-S^3E pulse scheme[12] (Figure S1A). The spectrum was acquired in ~7 min with 2 scans per row, 0.36 s recycle delay ($3 \times {}^{1}H\ T_1$), $t_{1,max}(^{15}N) = 25.6$ ms, and $t_{2,max}(^{13}C) = 30$ ms and processed with 81°-shifted sine-bell window functions in F_1 and F_2. (B) Representative strips from 3D $^{15}N-^{13}C\alpha-^{13}CO$ (NCACO; red contours) and $^{13}C\alpha-^{15}N-^{13}CO$ spectra (CANCO; blue contours) showing sequential backbone assignments for residues D36-W43, recorded using the pulse schemes in Figure S2. Each spectrum was acquired in ~2.9 h with 2 scans per row, 0.36 s recycle delay, $t_{1,max}(^{15}N) = 18.4$ ms, $t_{2,max}(^{13}C) = 8$ ms, and $t_{3,max}(^{13}C) = 30$ ms and processed with 81°-shifted sine-bell window functions in each dimension.

ratios range from 12 (T18N-T17CO) to 38 (K13N-L12CO) and the average *S/N* ratio was found to be 27 ± 6. Most importantly, a comparable 2D NCO spectrum, displaying signal intensities only ~25% lower on average, could be obtained for the fully protonated CN-28EDTA-Cu^{2+} sample in the same amount of time (Figure S4). Small regions from 3D CANCO and NCACO spectra recorded in ~2.9 h each, which enable complete sequential ^{15}N, ^{13}CO, and $^{13}C\alpha$ resonance assignments to be established for DCN-28EDTA-Cu^{2+}, are shown in Figure 1B, and additional data sets including 2D N(CA)CO and 3D CANCO, NCACO, and NCACB are shown in Figures S5−S7 for DCN- and CN-28EDTA-Cu^{2+}. Altogether, these data indicate that while a high degree of protein deuteration facilitates efficient ^{1}H decoupling and results in highest sensitivity spectra, it is not absolutely essential. Indeed, in most cases (3D NCACB being the main exception) 2D and 3D spectra of comparable quality could be recorded in approximately the same amount of time for the fully protonated protein, and as expected, deuteration afforded the largest sensitivity gains for correlations involving $^{13}CH_2$ groups (glycine Cα and most Cβ).

The ability to rapidly record high-quality 2D and 3D spectra of paramagnetic proteins has major practical consequences for protein structural studies based on SSNMR measurements of paramagnetic relaxation enhancements[10,11] and pseudocontact shifts.[13] To illustrate this, in Figure 2 we show site-specific measurements of backbone amide ^{15}N longitudinal relaxation rates[11,14] ($^{15}N\ R_1$) for DCN-28EDTA-Cu^{2+} and CN-8EDTA-Cu^{2+}. A comparison of $^{15}N\ R_1$ data for DCN-28EDTA-Cu^{2+} and CN-28EDTA-Cu^{2+} (Figure S8) reveals

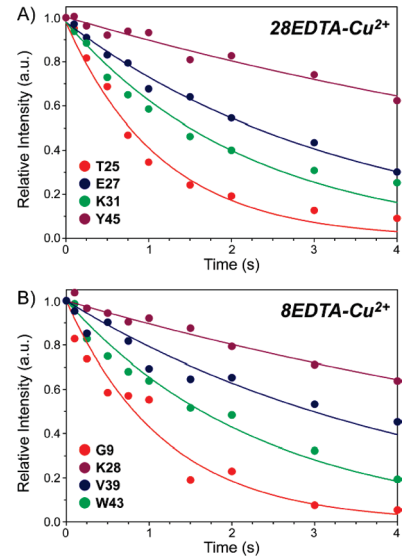

Figure 2. (A) Representative SSNMR measurements of backbone amide ^{15}N longitudinal relaxation rates, $R_1 = T_1^{-1}$, for residues T25, E27, K31, and Y45 in DCN-28EDTA-Cu^{2+}. Decaying single exponential fits are shown as solid lines. Spectra were recorded at 11.7 T and 40 kHz MAS using the pulse scheme in Figure S3. The experiment time was ~10 h. (B) Same as panel (A) for G9, K28, V39, and W43 in CN-8EDTA-Cu^{2+}.

that protein deuteration has a negligible effect on the measured longitudinal relaxation rates. The pseudo-3D SSNMR experiments, which consisted of a series of ten 2D NCO spectra with increasing ^{15}N longitudinal relaxation delays up to 4 s, could be recorded in as little as ~10 h per protein sample. Remarkably, previous measurements of this type performed using conventional SSNMR schemes at ~11 kHz MAS, which utilized ~7−8 times as much labeled protein and contained fewer points in the ^{15}N relaxation dimension, required ~2−4 days of measurement time to achieve comparable results.[11] The significant dispersion in the measured backbone amide $^{15}N\ R_1$ rates is primarily related to the proximity of the ^{15}N nuclei to the Cu^{2+} ion. For instance, while for 28EDTA-Cu^{2+} the α-helical amino acid residues, A24-Q32, display significantly elevated relaxation rates (cf., Figures 2A and S8A), they are among the slowest relaxing amino acids in 8EDTA-Cu^{2+} as illustrated by the relaxation trajectory for K28 in Figure 2B. In contrast, for 8EDTA-Cu^{2+} the largest relaxation rates are found for residues located in strands $\beta1-\beta4$, in proximity to the Cu^{2+} center.

To quantitatively assess the paramagnetic contributions to ^{15}N longitudinal relaxation rates due to the presence of Cu^{2+} ions, analogous relaxation trajectories were recorded for the corresponding diamagnetic control samples, DCN-28EDTA-Zn^{2+} and CN-8EDTA-Zn^{2+} (representative trajectories are shown in Figures S10 and S11). For each residue the longitudinal ^{15}N paramagnetic relaxation enhancement (Γ_1^N) is obtained by taking the difference between the $^{15}N\ R_1$ values for EDTA-Cu^{2+} and EDTA-Zn^{2+} proteins, found by modeling the relaxation trajectories as single exponential decays. Figure 3 shows the ^{15}N longitudinal PREs for 28EDTA-Cu^{2+} and 8EDTA-Cu^{2+} as a function of residue number and location within the three-dimensional protein structure. The observed Γ_1^N values range between ~0.03 and 0.8 s^{-1}, and as expected, the PRE magnitudes are highly correlated with the $^{15}N-Cu^{2+}$ separation. Additionally, the residue-specific ^{15}N PRE measurements permit distances between the Cu^{2+} ion and backbone amide ^{15}N nuclei to be estimated as described previously[11] by using the Solomon−Bloembergen equation[15] (cf., Tables S1 and S2).

To evaluate the potential of the measured ^{15}N PREs and $^{15}N-Cu^{2+}$ distances to yield useful structural information, in Figure 4A we show the comparison of the experimentally observed Γ_1^N values and the corresponding values calculated from structural models of 8EDTA-

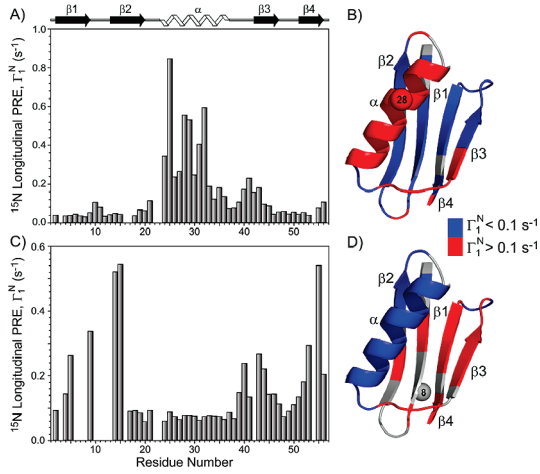

Figure 3. (A) Backbone amide ^{15}N longitudinal paramagnetic relaxation enhancements, $\Gamma_1^N = R_1(Cu^{2+}) - R_1(Zn^{2+})$, for DCN-28EDTA-Cu^{2+} as a function of residue number. Γ_1^N was set to zero for residues where quantitative measurement was not possible due to insufficient spectral resolution. (B) Ribbon diagram of GB1 (PDB entry 1PGA) with Γ_1^N values mapped onto the structure. Residues with $\Gamma_1^N < 0.1$ s^{-1} (corresponding to ^{15}N−Cu^{2+} distances, $r_{N-Cu} > \sim 15$ Å) and $\Gamma_1^N > 0.1$ s^{-1} ($r_{N-Cu} < \sim 15$ Å) are highlighted in blue and red, respectively, and residues for which Γ_1^N was not determined are colored in gray. The residue containing the EDTA-Cu^{2+} side chain is indicated by a sphere. (C,D) Same as panels (A,B) for CN-8EDTA-Cu^{2+}.

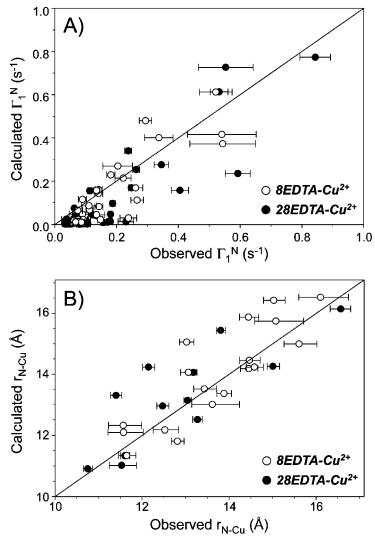

Figure 4. Comparison between the experimentally determined (A) ^{15}N longitudinal PREs and (B) ^{15}N−Cu^{2+} distances, and corresponding values calculated from structural models of 8EDTA-Cu^{2+} and 28EDTA-Cu^{2+}.

Cu^{2+} and 28EDTA-Cu^{2+}, constructed based on the atomic coordinates of wild-type GB1 using Xplor-NIH.[16] Overall, the experimental PREs are found to be in good agreement with those predicted from the protein structural models, with a root-mean-squared (rms) deviation of ∼0.09 s^{-1}. The largest deviations are seen for a cluster of measurements corresponding to the smallest calculated Γ_1^N values ($\Gamma_1^N < 0.05$ s^{-1}, associated with the longest ^{15}N−Cu^{2+} distances, $r_{N-Cu} > 17$ Å), where the experimentally observed PREs systematically exceed those predicted by the protein structural models. As discussed previously,[11] these systematic deviations most likely reflect contributions from residual intermolecular ^{15}N−Cu^{2+} couplings due to insufficient dilution of EDTA-Cu^{2+} proteins in the diamagnetic matrix. In contrast, the agreement between the observed and expected ^{15}N PREs, and, especially, ^{15}N−Cu^{2+} distances (note that for the larger PRE values, the PRE is a highly sensitive function of the ^{15}N−Cu^{2+} distance; e.g., PREs of 0.2 and 0.6 correspond to distances of ca. 13.5 and 11.5 Å, respectively), is substantially improved for measurements corresponding to Γ_1^N calculated > 0.05 s^{-1}. Figure 4B shows a set of ∼30 distance measurements in 8EDTA-Cu^{2+} and 28EDTA-Cu^{2+} that fall into this category. These data reveal a strong correlation between the measured and predicted ^{15}N−Cu^{2+} distances, with an rms deviation of ∼0.9 Å, indicating that such distance restraints can be suitable for applications to SSNMR protein structure refinement.

In conclusion, we have demonstrated that a condensed data acquisition approach[5] that uses covalently bound paramagnetic tags to enhance ^{1}H spin−lattice relaxation facilitates acquisition of high resolution and sensitivity MAS SSNMR spectra in as little as several minutes for protein samples containing only ∼0.1−0.2 μmol of ^{13}C,^{15}N- or ^{2}H,^{13}C,^{15}N-labeled protein. Most significantly, this mode of data collection is naturally suited toward structural SSNMR studies of paramagnetic proteins based on measurements of pseudocontact shifts and nuclear PREs,[10,11,13] as illustrated here for two paramagnetic mutants of protein GB1. In addition, the possibility of being able to modulate protein ^{1}H T_1 times by directly embedding regularly spaced paramagnetic moieties at specific sites in the protein lattice promises to be a generally applicable tool for enhancing the sensitivity of MAS NMR spectra of natively diamagnetic proteins found in a variety of environments, which may pose challenges for traditional PACC schemes based on external paramagnetic doping,[5,7] including large supramolecular aggregates and biological membranes.

Acknowledgment. This work was supported by the National Science Foundation (CAREER Award MCB-0745754 to C.P.J.). We thank Dr. Charles Schwieters for assistance with Xplor-NIH.

Supporting Information Available: Experimental section, pulse scheme diagrams, additional NMR spectra, relaxation trajectories, and tables. This material is available free of charge via the Internet at http://pubs.acs.org.

References

(1) McDermott, A. *Annu. Rev. Biophys.* **2009**, *38*, 385–403. Lange, A.; Giller, K.; Hornig, S.; Martin-Eauclaire, M. F.; Pongs, O.; Becker, S.; Baldus, M. *Nature* **2006**, *440*, 959–962. Wasmer, C.; Lange, A.; Van Melckebeke, H.; Siemer, A. B.; Riek, R.; Meier, B. H. *Science* **2008**, *319*, 1523–1526. Helmus, J. J.; Surewicz, K.; Nadaud, P. S.; Surewicz, W. K.; Jaroniec, C. P. *Proc. Natl. Acad. Sci. U.S.A.* **2008**, *105*, 6284–6289.
(2) Pines, A.; Gibby, M. G.; Waugh, J. S. *J. Chem. Phys.* **1973**, *59*, 569–590.
(3) Ganapathy, S.; Naito, A.; McDowell, C. A. *J. Am. Chem. Soc.* **1981**, *103*, 6011–6015.
(4) Bloembergen, N. *Physica* **1949**, *15*, 386–426.
(5) Wickramasinghe, N. P.; Kotecha, M.; Samoson, A.; Past, J.; Ishii, Y. *J. Magn. Reson.* **2007**, *184*, 350–356. Wickramasinghe, N. P.; Parthasarathy, S.; Jones, C. R.; Bhardwaj, C.; Long, F.; Kotecha, M.; Mehboob, S.; Fung, L. W. M.; Past, J.; Samoson, A.; Ishii, Y. *Nat. Methods* **2009**, *6*, 215–218.
(6) Ernst, M.; Meier, M. A.; Tuherm, T.; Samoson, A.; Meier, B. H. *J. Am. Chem. Soc.* **2004**, *126*, 4764–4765. Vijayan, V.; Demers, J. P.; Biernat, J.; Mandelkow, E.; Becker, S.; Lange, A. *ChemPhysChem* **2009**, *10*, 2205–2208.
(7) Linser, R.; Chevelkov, V.; Diehl, A.; Reif, B. *J. Magn. Reson.* **2007**, *189*, 209–216.
(8) Laage, S.; Sachleben, J. R.; Steuernagel, S.; Pierattelli, R.; Pintacuda, G.; Emsley, L. *J. Magn. Reson.* **2009**, *196*, 133–141. Bertini, I.; Emsley, L.; Lelli, M.; Luchinat, C.; Mao, J.; Pintacuda, G. *J. Am. Chem. Soc.* **2010**, *132*, 5558–5559.
(9) Yamamoto, K.; Xu, J.; Kawulka, K. E.; Vederas, J. C.; Ramamoorthy, A. *J. Am. Chem. Soc.* **2010**, *132*, 6929–6931.
(10) Nadaud, P. S.; Helmus, J. J.; Hofer, N.; Jaroniec, C. P. *J. Am. Chem. Soc.* **2007**, *129*, 7502–7503.
(11) Nadaud, P. S.; Helmus, J. J.; Kall, S. L.; Jaroniec, C. P. *J. Am. Chem. Soc.* **2009**, *131*, 8108–8120.
(12) Laage, S.; Lesage, A.; Emsley, L.; Bertini, I.; Felli, I. C.; Pierattelli, R.; Pintacuda, G. *J. Am. Chem. Soc.* **2009**, *131*, 10816–10817.
(13) Balayssac, S.; Bertini, I.; Lelli, M.; Luchinat, C.; Maletta, M. *J. Am. Chem. Soc.* **2007**, *129*, 2218–2219. Balayssac, S.; Bertini, I.; Bhaumik, A.; Lelli, M.; Luchinat, C. *Proc. Natl. Acad. Sci. U.S.A.* **2008**, *105*, 17284–17289.
(14) Giraud, N.; Bockmann, A.; Lesage, A.; Penin, F.; Blackledge, M.; Emsley, L. *J. Am. Chem. Soc.* **2004**, *126*, 11422–11423.
(15) Solomon, I. *Phys. Rev.* **1955**, *99*, 559–565. Bloembergen, N.; Morgan, L. O. *J. Chem. Phys.* **1961**, *34*, 842–850.
(16) Schwieters, C. D.; Kuszewski, J. J.; Tjandra, N.; Clore, G. M. *J. Magn. Reson.* **2003**, *160*, 65–73.

JA103545E

Supporting Information

Rapid Acquisition of Multidimensional Solid-State NMR Spectra of Proteins Facilitated by Covalently Bound Paramagnetic Tags

Philippe S. Nadaud, Jonathan J. Helmus, Ishita Sengupta and Christopher P. Jaroniec*

Department of Chemistry, The Ohio State University, Columbus, Ohio 43210
E-mail: jaroniec@chemistry.ohio-state.edu

Experimental Section

Protein Expression, Purification and Incorporation of EDTA-Cu^{2+}/Zn^{2+} Side-Chains. The plasmid DNA encoding for the K28C mutant of GB1 was described previously.[1] The N8C-GB1 plasmid was constructed in similar fashion by using the GB1 plasmid DNA (kindly provided by Dr. Angela Gronenborn), appropriate primers (Sigma-Aldrich) and the QuikChange II site-directed mutagenesis kit (Stratagene), and the sequence identity confirmed by DNA sequencing (GENEWIZ, South Plainfield, NJ). Below we describe the details of protein samples prepared starting with the K28C-GB1 plasmid, and note that identical procedures were used to prepare the N8C-GB1-based samples.

^{13}C,^{15}N-enriched K28C-GB1 was overexpressed in *Escherichia coli* in minimal medium containing 1 g/L $^{15}NH_4Cl$ and 3 g/L ^{13}C-glucose (Cambridge Isotope Laboratories); for the expression of ^{2}H,^{13}C,^{15}N-labeled protein the minimal medium was prepared in D_2O and contained 1 g/L $^{15}NH_4Cl$ and 3 g/L ^{2}H,^{13}C-glucose. Proteins were purified in H_2O-based buffers by using a combination of heat treatment at 80°C and size exclusion chromatography[1]—this resulted in incorporation of ^{1}H nuclei at all exchangeable sites for ^{2}H,^{13}C,^{15}N-labeled K28C-GB1—and routinely characterized by SDS-PAGE, mass spectrometry and solution-state NMR. The thiol-specific disulfide reagent, N-[S-(2-pyridylthio)cysteaminyl]EDTA[2] (Toronto Research Chemicals), pre-loaded with Cu^{2+}, was used to incorporate the EDTA-Cu^{2+} side-chain at residue 28 as described previously,[3] and an analogous procedure was used to prepare ^{13}C,^{15}N- and ^{2}H,^{13}C,^{15}N-labeled diamagnetic control protein samples containing EDTA-Zn^{2+} side-chains. For brevity, the EDTA-Cu^{2+} and EDTA-Zn^{2+} modified K28C-GB1 proteins are referred to as 28EDTA-Cu^{2+} and 28EDTA-Zn^{2+}, respectively (the corresponding N8C-GB1 samples are 8EDTA-Cu^{2+} and 8EDTA-Zn^{2+}).

Preparation of Protein Samples for Solid-State NMR. Microcrystalline protein samples for solid-state NMR analysis consisted of ^{13}C,^{15}N- or ^{2}H,^{13}C,^{15}N-28EDTA-Cu^{2+} co-precipitated with natural abundance GB1 in a 28EDTA-Cu^{2+}:GB1 molar ratio of ~1:3, and were prepared by using microdialysis at 4°C with a precipitant solution containing 2-methylpentane-2,4-diol, isopropanol, and deionized water in a 2:1:1 (v/v) ratio as described previously.[3] Protein microcrystals were packed into 1.6 mm Varian (Palo Alto, CA) zirconia rotors. The final NMR samples contained 1.0 ± 0.1 mg (~150 nmol) of ^{13}C,^{15}N-28EDTA-Cu^{2+} and 1.1 ± 0.1 mg (~150 nmol) of ^{2}H,^{13}C,^{15}N-28EDTA-Cu^{2+}, as determined by the quantitative comparison of spectral intensities in fully-relaxed ^{13}C Bloch decay spectra for the labeled proteins and a control sample containing a known amount of uniformly ^{13}C,^{15}N-labeled L-threonine.

Solid-State NMR Spectroscopy. Experiments were performed on a three-channel 11.7 T Varian spectrometer operating at frequencies of 499.8 MHz for ^{1}H, 125.7 MHz for ^{13}C and 50.6 MHz for ^{15}N, and equipped with a 1.6 mm Varian FastMAS™ probe. The MAS frequency was set to 40 kHz and regulated to ca. ± 20 Hz using a Varian MAS control unit. The sample temperature was controlled by using a stream of compressed air delivered to the sample at a flow rate of ~30 L/min through a variable temperature stack. The compressed air temperature was set to -30°C resulting in an effective sample temperature of ~5°C as determined by lead nitrate calibration (data courtesy of Dr. John Stringer, Varian Inc.). NMR spectra were processed using NMRPipe[4] and analyzed with NMRDraw[4] and Sparky.[5] The experimental NMR parameters and pulse sequences used are described in detail in the figure captions.

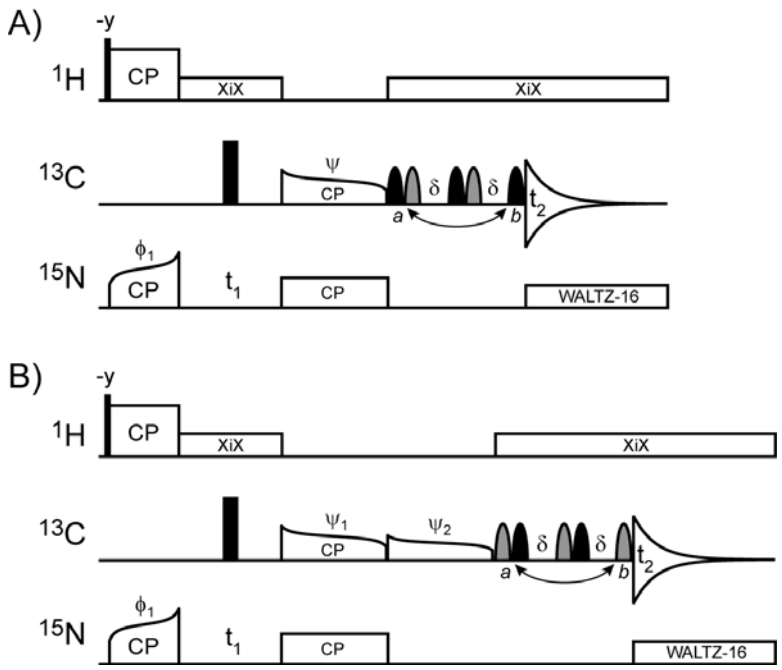

Figure S1. Pulse schemes of the 2D NCO-S^{3}E **(A)** and 2D N(CA)CO-S^{3}E **(B)** experiments. The experimental parameters listed for these and all other pulse schemes (c.f., Figures S2 and S3) are for a MAS rate of 40 kHz employed in this work. Narrow and wide black rectangles correspond to 90^o and 180^o pulses, and all pulses have phase *x* unless indicated otherwise. ^{1}H-^{15}N cross-polarization[6] (CP) was achieved using a ~100 kHz ^{1}H field, ~60 kHz ^{15}N field (with tangent ramp[7]), and contact time of 1 ms. XiX[8] ^{1}H and WALTZ-16[9] ^{15}N decoupling was applied as indicated at field strengths of ~11 kHz and ~3.3 kHz, respectively. **(A)** 2D NCO-S^{3}E: The ^{1}H, ^{13}C and ^{15}N carriers were placed at 4.7, 175, and 120 ppm, respectively. ^{15}N-^{13}CO SPECIFIC CP[10] employed a ~15 kHz ^{15}N field, ~25 kHz ^{13}C field (with tangent ramp), and a 5 ms contact time. ^{13}CO-^{13}Cα J-decoupling during ^{13}CO detection was achieved using the S^{3}E scheme[11] with the delay δ = 2.25 ms, by recording two separate spectra with the frequency-selective ^{13}CO 180^o pulses (applied on-resonance at the frequency of 175 ppm; filled black shapes) and ^{13}Cα 180^o pulses (applied off-resonance at the frequency of 55 ppm; filled gray shapes) in position *a* or *b*, and processing the data as described by Laage et al.[11] The selective ^{13}CO and ^{13}Cα 180^o pulses were of the rSNOB type[12] and had durations of 250 μs. Note that for spectrum *b* the ^{13}Cα selective pulse is applied immediately following the ^{13}C spin-lock pulse (see ref. [11] for details). The following minimal two-step phase cycles were employed to record spectra *a* and *b*. Spectrum *a*: $\phi_1 = x, -x$; $\psi = x$; receiver = *x, -x*. Spectrum *b*: $\phi_1 = x, -x$; $\psi = -y$; receiver = *x, -x*. For spectra *a* and *b* quadrature in the ^{15}N dimension was achieved by alternating phase ϕ_1 according to the States method.[13] **(B)** 2D N(CA)CO-S^{3}E: The ^{1}H, ^{13}C and ^{15}N carriers were placed at 4.7, 55, and 120 ppm, respectively. ^{15}N-^{13}Cα SPECIFIC CP employed a ~15 kHz ^{15}N field, ~25 kHz ^{13}C field (with tangent ramp), and a 7.5 ms contact time. ^{13}Cα-^{13}CO magnetization transfer was achieved using a ~20 kHz ^{13}C field[14] (tangent ramp) with duration of 5 ms. ^{13}CO-^{13}Cα J-decoupling during ^{13}CO detection was achieved using the S^{3}E scheme as described above, with the only exceptions being that the selective ^{13}CO 180^o pulses (filled gray shapes) were applied off-resonance at the frequency of 175 ppm and the ^{13}Cα 180^o pulses (filled black shapes) were applied on-resonance at the frequency of 55 ppm. The following minimal two-step phase cycles were employed to record spectra *a* and *b*. Spectrum *a*: $\phi_1 = x, -x$; $\psi_1 = x$; $\psi_2 = x$; receiver = *x, -x*. Spectrum *b*: $\phi_1 = x, -x$; $\psi_1 = -y$; $\psi_2 = -y$; receiver = *x, -x*. For spectra *a* and *b* quadrature in the ^{15}N dimension was achieved by alternating phase ϕ_1 according to the States method.

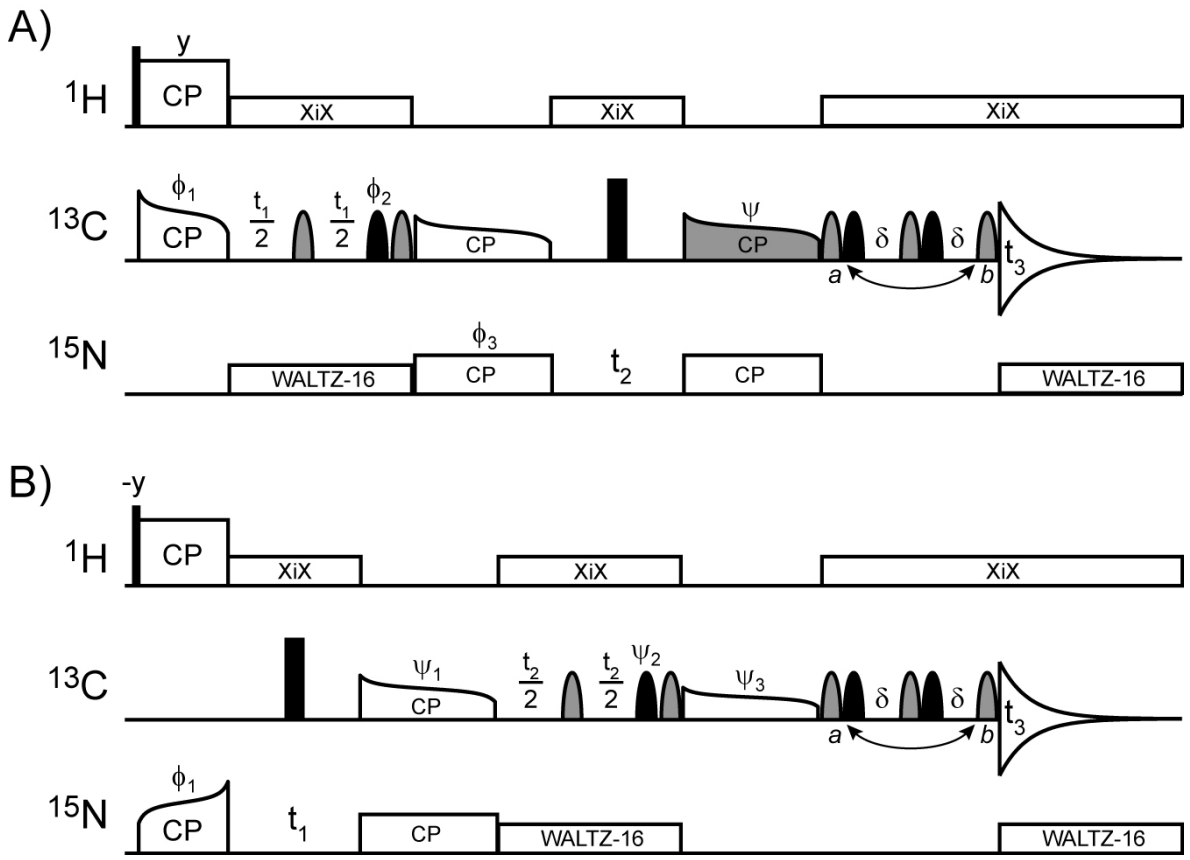

Figure S2. Pulse schemes of the 3D CANCO-S^{3}E **(A)** and 3D NCACO-S^{3}E **(B)** experiments. For both experiments the ^{1}H, ^{13}C and ^{15}N carriers were placed at 4.7, 55, and 120 ppm, respectively. Narrow and wide black rectangles correspond to 90^o and 180^o pulses, and all pulses have phase *x* unless indicated otherwise. Filled black shapes correspond to frequency-selective ^{13}Cα 180^o pulses (rSNOB, 250 μs) applied on-resonance at the frequency of 55 ppm, and filled gray shapes correspond to ^{13}CO 180^o pulses (rSNOB, 250 μs) applied off-resonance at the frequency of 175 ppm. Most of the experimental parameters, including (where applicable) the durations and field strengths for ^{1}H-^{15}N, ^{15}N-^{13}Cα and ^{13}Cα-^{13}CO magnetization transfers and ^{1}H and ^{15}N decoupling, as well as the S^{3}E parameters are identical to those used for the pulse scheme described in Figure S1B. **(A)** 3D CANCO-S^{3}E: ^{1}H-^{13}C CP was achieved using a ~100 kHz ^{1}H field, ~60 kHz ^{13}C field (with tangent ramp), and contact time of 1.6 ms. ^{15}N-^{13}CO SPECIFIC CP employed a ~15 kHz ^{15}N field, ~25 kHz ^{13}C field (applied off-resonance at the frequency of 175 ppm with a tangent ramp; indicated by a filled gray shape), and a 5 ms contact time. The following minimal two-step phase cycles were employed to record spectra *a* and *b*. Spectrum *a*: $\phi_1 = x$; $\phi_2 = x, y$; $\phi_3 = x$; $\psi = y$; receiver = *x*, *-x*. Spectrum *b*: $\phi_1 = x$; $\phi_2 = x, y$; $\phi_3 = x$; $\psi = -x$; receiver = *x*, *-x*. For spectra *a* and *b* quadrature in the ^{13}Cα and ^{15}N dimensions was achieved by alternating phases ϕ_1 and ϕ_3, respectively, according to the States method. **(B)** 3D NCACO-S^{3}E: The following minimal two-step phase cycles were employed to record spectra *a* and *b*. Spectrum *a*: $\phi_1 = x$; $\psi_1 = x$; $\psi_2 = x, y$; $\psi_3 = x$; receiver = *x*, *-x*. Spectrum *b*: $\phi_1 = x$; $\psi_1 = -y$; $\psi_2 = -y, x$; $\psi_3 = -y$; receiver = *x*, *-x*. For spectra *a* and *b* quadrature in the ^{15}N and ^{13}Cα dimensions was achieved by alternating phases ϕ_1 and ψ_1, respectively, according to the States method.

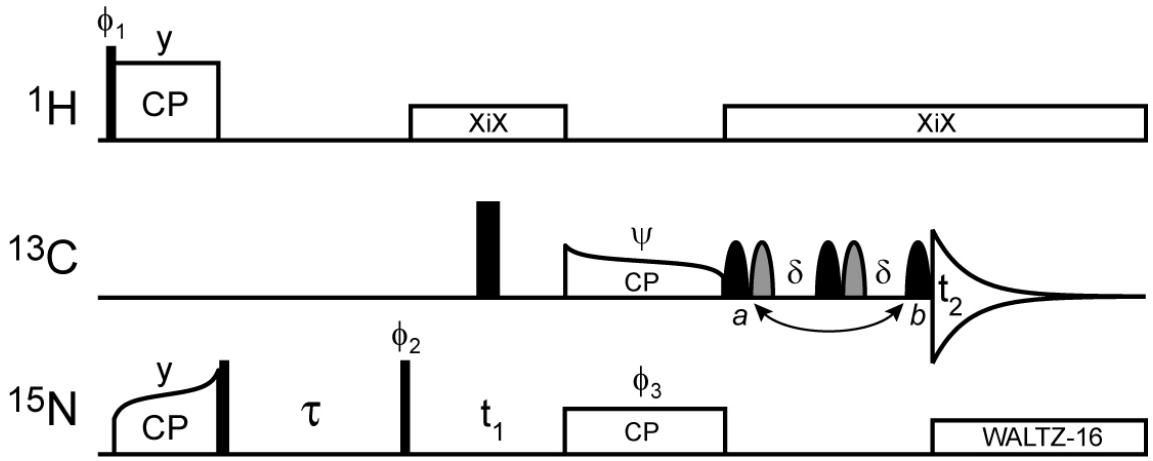

Figure S3. 2D NCO-S^{3}E based pulse scheme for the site-resolved measurement of ^{15}N R_1 relaxation rate constants.[15] Most of the experimental parameters are identical to those for the pulse scheme in Figure S1A. The following phase cycles were employed to record spectra *a* and *b*. Spectrum *a*: ϕ_1 = 2(*x*), 2(-*x*); ϕ_2 = *x*, -*x*; ϕ_3 = *y*; ψ = *x*; receiver = *x*, -*x*, -*x*, *x*. Spectrum *b*: ϕ_1 = 2(*x*), 2(-*x*); ϕ_2 = *x*, -*x*; ϕ_3 = *y*; ψ = -*y*; receiver = *x*, -*x*, -*x*, *x*. For spectra *a* and *b* quadrature in the ^{15}N dimension was achieved by alternating phase ϕ_2 according to the States method.

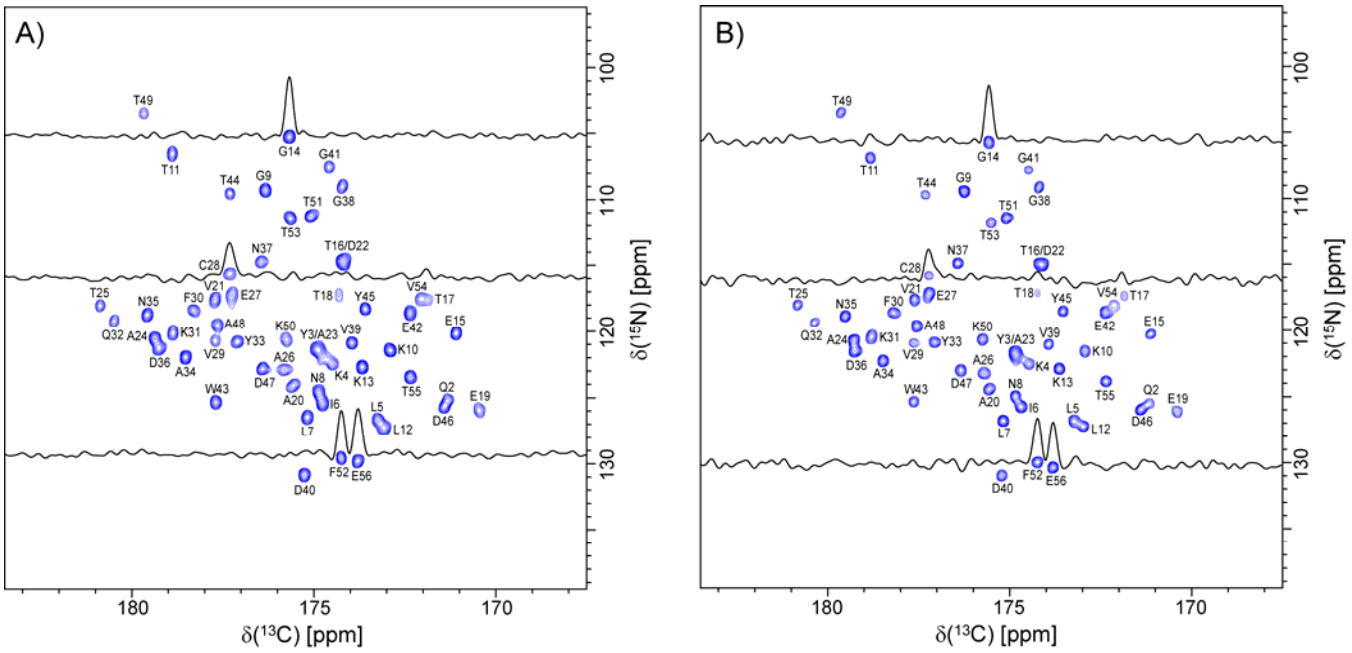

Figure S4. 2D NCO spectra of **(A)** $^{2}H,^{13}C,^{15}N$-28EDTA-Cu^{2+} (1.1 mg, ~150 nmol) back-exchanged with H_2O (c.f., Figure 1) and **(B)** $^{13}C,^{15}N$-28EDTA-Cu^{2+} (1.0 mg, ~150 nmol), recorded at 11.7 T and 40 kHz MAS using the 2D NCO-S^3E pulse scheme described in Figure S1A. Both spectra were recorded under identical conditions with 2 scans per row, 0.36 s recycle delay (~3×^{1}H T_1), $t_{1,max}(^{15}N)$ = 25.6 ms, $t_{2,max}(^{13}C)$ = 30 ms, total experiment time ~7 minutes, and processed with 81°-shifted sine-bell window functions in F_1 and F_2.

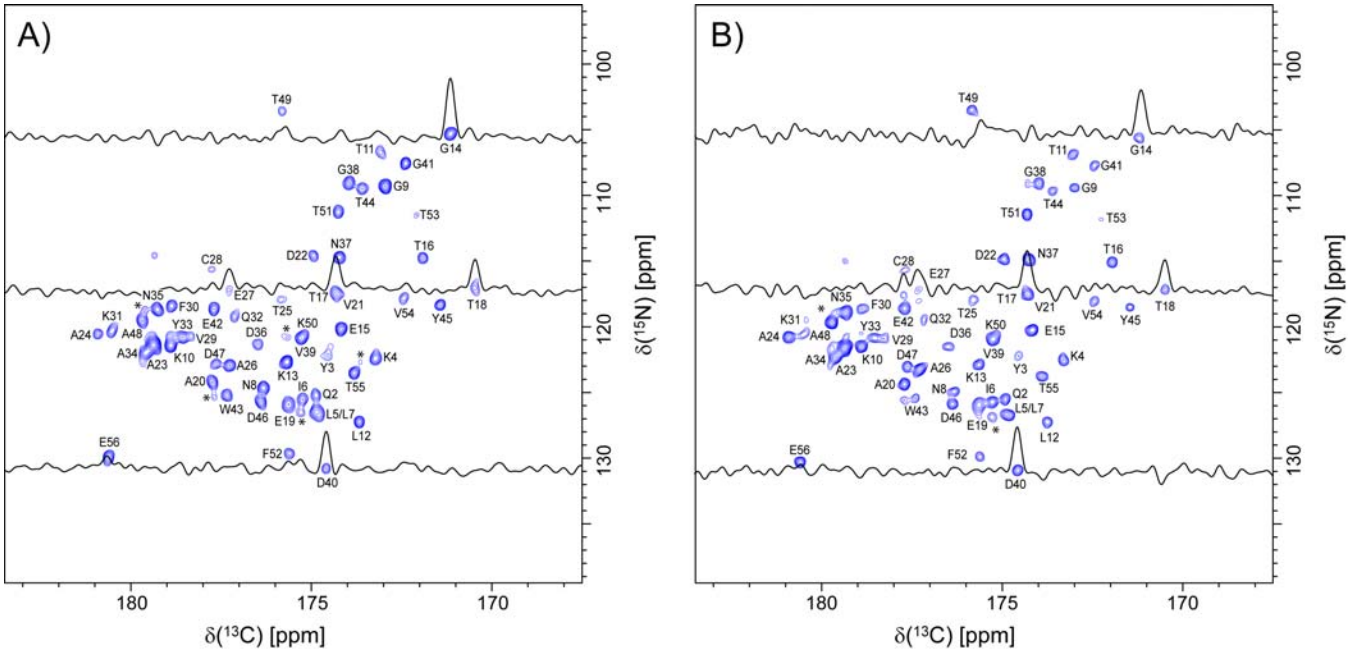

Figure S5. 2D N(CA)CO spectra of **(A)** $^{2}H,^{13}C,^{15}N$-28EDTA-Cu^{2+} (1.1 mg, ~150 nmol) back-exchanged with H_2O and **(B)** $^{13}C,^{15}N$-28EDTA-Cu^{2+} (1.0 mg, ~150 nmol), recorded at 11.7 T and 40 kHz MAS using the 2D N(CA)CO-S^3E pulse scheme described in Figure S1B. Both spectra were recorded under identical conditions with 2 scans per row, 0.36 s recycle delay (~3×^{1}H T_1), $t_{1,max}(^{15}N)$ = 25.6 ms, $t_{2,max}(^{13}C)$ = 30 ms, total experiment time ~30 minutes, and processed with 81°-shifted sine-bell window functions in F_1 and F_2. The major cross-peaks, corresponding to intra-residue ^{15}N-^{13}CO correlations, are labeled by residue number. Minor inter-residue correlations are indicated by asterisks.

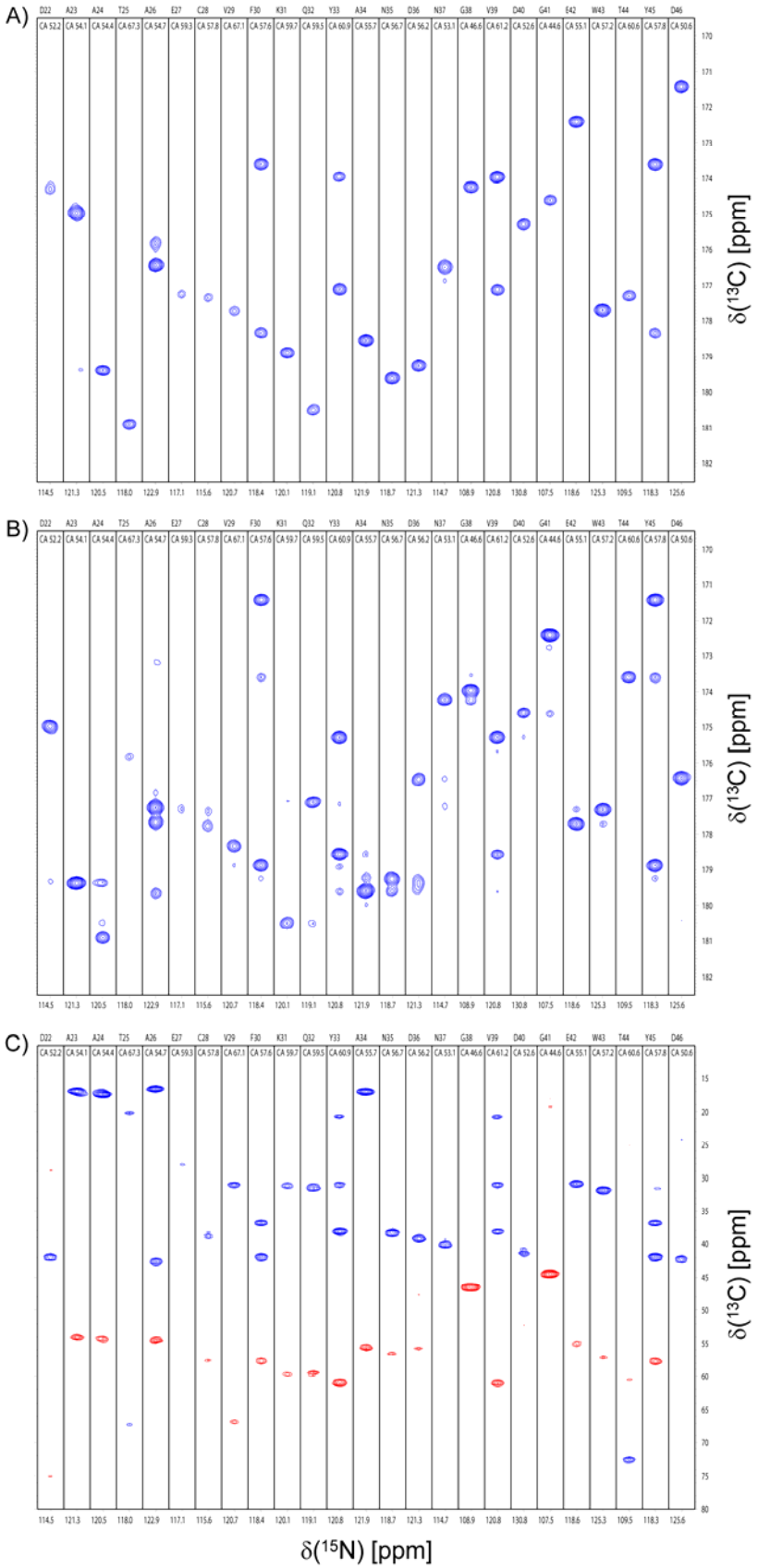

Figure S6. Representative strips from 3D **(A)** CANCO, **(B)** NCACO and **(C)** NCACB spectra of $^{2}H,^{13}C,^{15}N$-28EDTA-Cu^{2+} (1.1 mg, ~150 nmol) back-exchanged with H_2O, acquired at 11.7 T and 40 kHz MAS. **(A)** 3D CANCO: The spectrum was recorded using the 3D CANCO-S^3E pulse scheme

described in Figure S2A with 2 scans per row, 0.36 s recycle delay, $t_{1,max}(^{15}N)$ = 18.4 ms, $t_{2,max}(^{13}C)$ = 8 ms, $t_{3,max}(^{13}C)$ = 30 ms, total experiment time of ~2.9 hours, and processed with 81°-shifted sine-bell window functions in each dimension. **(B)** 3D NCACO: The spectrum was recorded using the 3D NCACO-S^3E pulse scheme described in Figure S2B with 2 scans per row, 0.36 s recycle delay, $t_{1,max}(^{15}N)$ = 18.4 ms, $t_{2,max}(^{13}C)$ = 8 ms, $t_{3,max}(^{13}C)$ = 30 ms, total experiment time of ~2.9 hours, and processed with 81°-shifted sine-bell window functions in each dimension. **(C)** 3D NCACB: The spectrum was recorded using a pulse scheme nearly identical to that shown in Figure S2B, with the exception that the ^{13}C-^{13}C magnetization transfer pulse parameters were set to emphasize $^{13}C\alpha$-$^{13}C\beta$ transfers instead of $^{13}C\alpha$-^{13}CO and no S^3E filter was used, with 2 scans per row, 0.36 s recycle delay, $t_{1,max}(^{15}N)$ = 18.4 ms, $t_{2,max}(^{13}C)$ = 8 ms, $t_{3,max}(^{13}C)$ = 20 ms, total experiment time of ~2.9 hours, and processed with 81°-shifted sine-bell window functions in F_1 and F_2, and a 81°-shifted squared sine-bell window function in F_3.

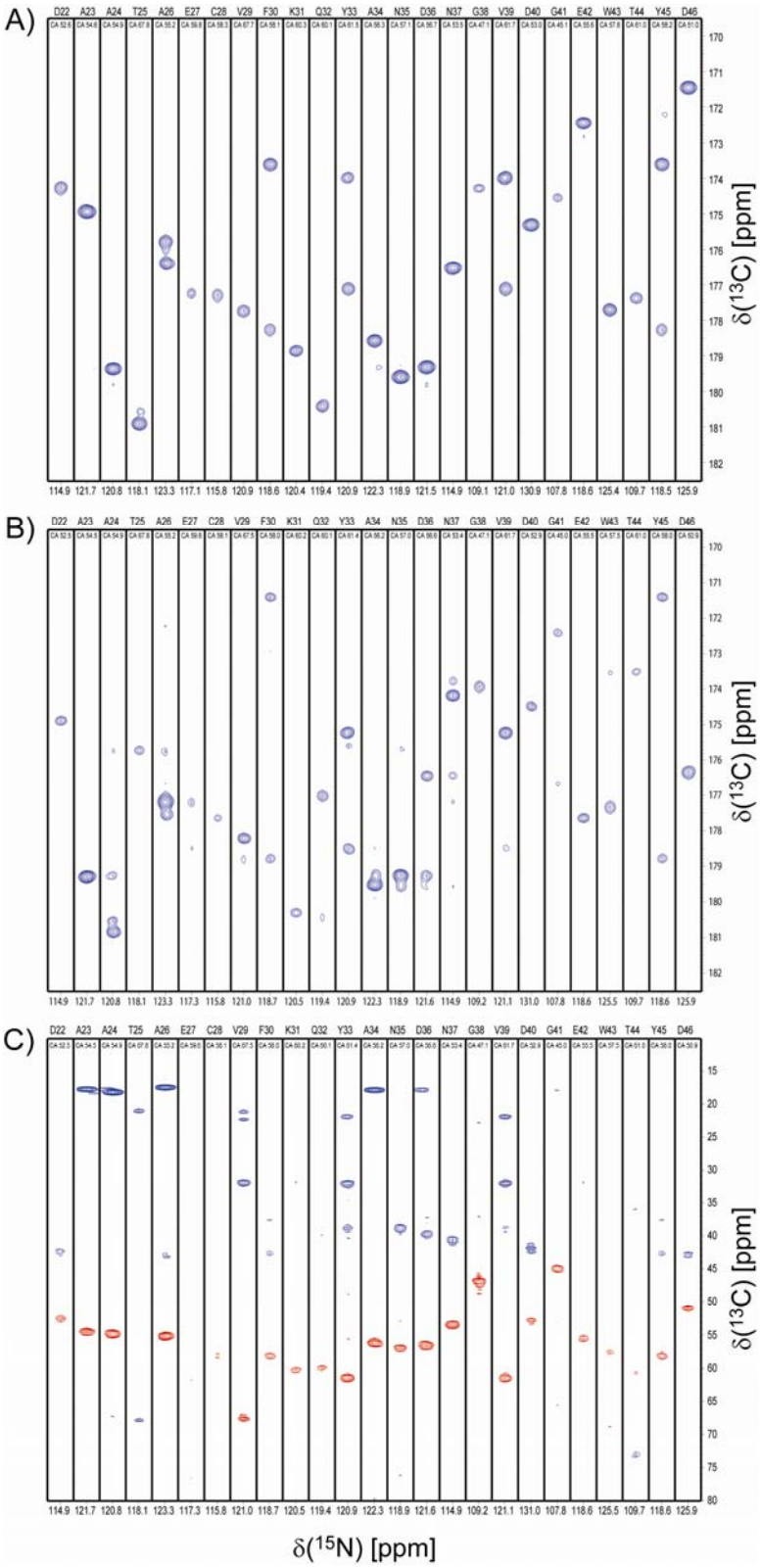

Figure S7. Representative strips from 3D **(A)** CANCO, **(B)** NCACO and **(C)** NCACB spectra of $^{13}C,^{15}N$-28EDTA-Cu^{2+} (1.0 mg, ~150 nmol) acquired at 11.7 T and 40 kHz MAS. All acquisition and processing parameters were the same as those used to record the spectra in Figure S6, except that 4, 4 and 16 scans per row were used for CANCO, NCACO and NCACB spectra, respectively, resulting in total experiment times of ca. 5.8, 5.8 and 23.2 hours, respectively.

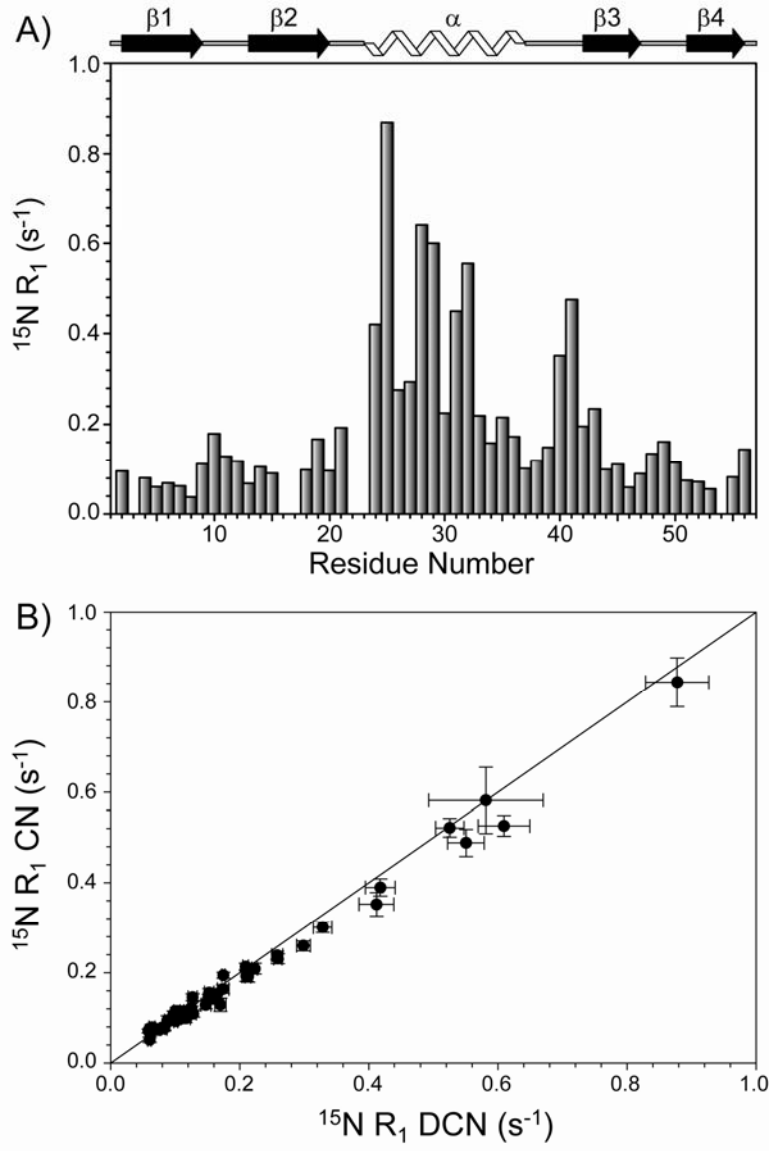

Figure S8. (A) Plot of backbone amide ^{15}N longitudinal relaxation rates, ^{15}N R_1, as a function of residue number for ^{2}H,^{13}C,^{15}N (DCN) labeled 28EDTA-Cu^{2+} (see Figure 2 for representative relaxation trajectories and additional details). **(B)** Comparison of ^{15}N R_1 values determined in DCN-28EDTA-Cu^{2+} and ^{13}C,^{15}N (CN) labeled 28EDTA-Cu^{2+}.

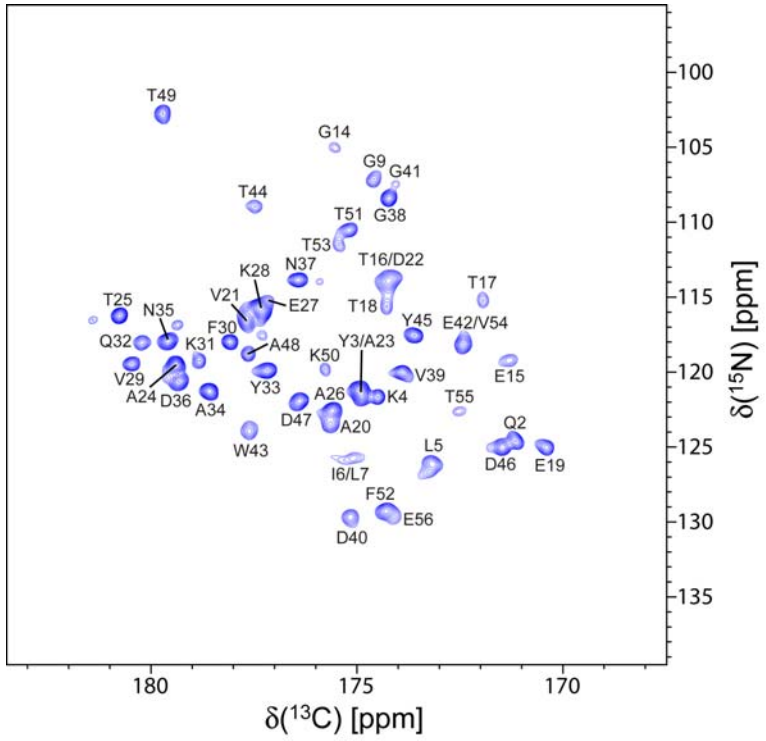

Figure S9. 2D NCO spectrum of $^{13}C,^{15}N$-8EDTA-Cu^{2+} recorded at 11.7 T and 40 kHz MAS using the 2D NCO-S^3E pulse scheme in Figure S1A. Resonance assignments were obtained by using a set of 3D chemical shift correlation experiments described in detail for 28EDTA-Cu^{2+}.

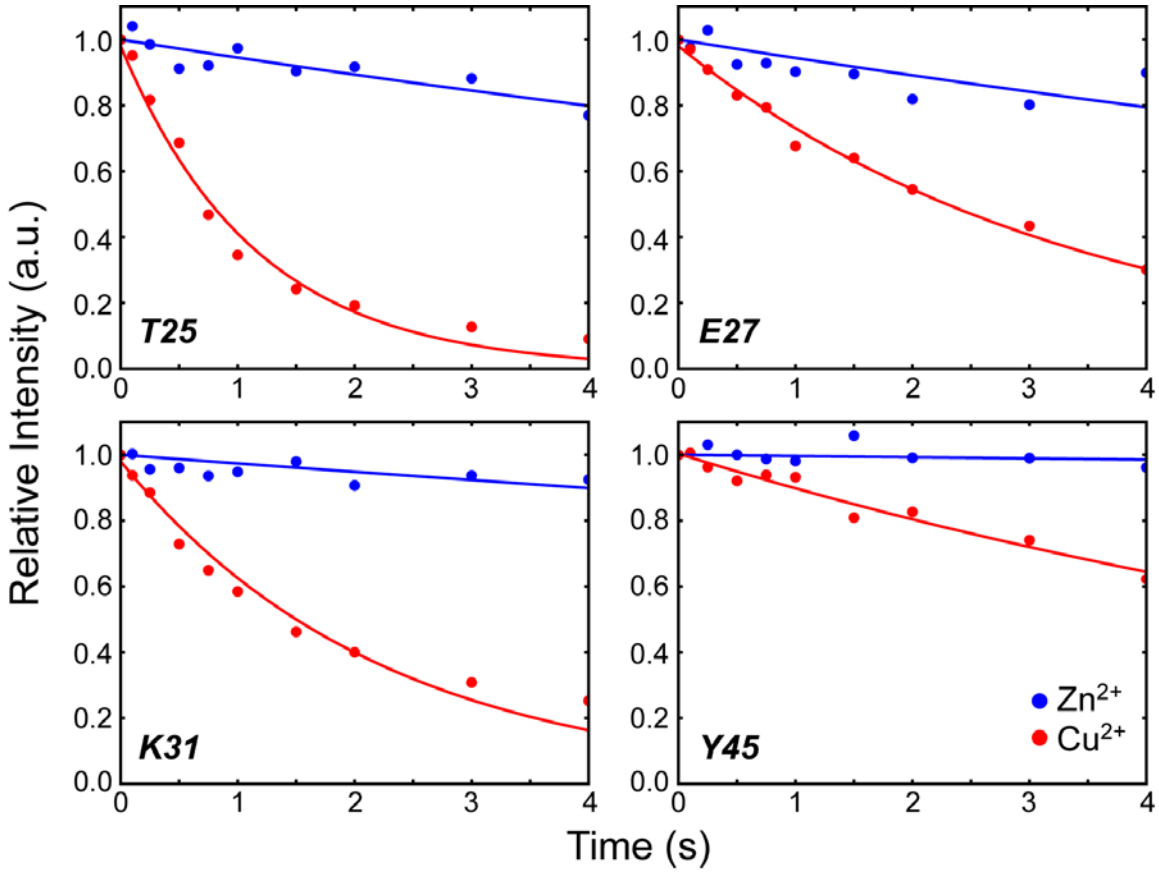

Figure S10. Representative measurements of residue-specific ^{15}N longitudinal relaxation rates in DCN-28EDTA-Cu^{2+} (red circles) and DCN-28EDTA-Zn^{2+} (blue circles), obtained using the pulse scheme in Figure S3 (see Figure 2 for additional details). Best fits to decaying single exponentials are shown as solid lines.

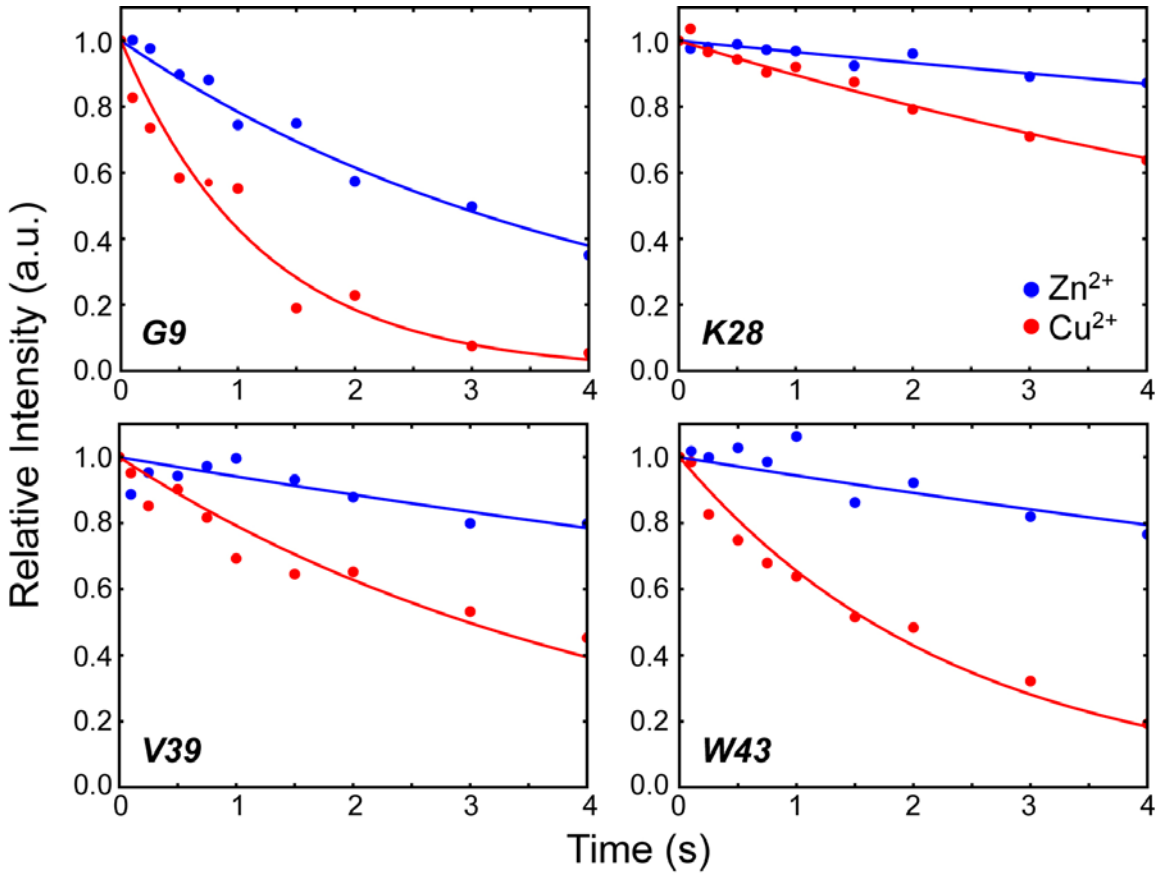

Figure S11. Representative measurements of residue-specific ^{15}N longitudinal relaxation rates in CN-8EDTA-Cu^{2+} (red circles) and CN-8EDTA-Zn^{2+} (blue circles), obtained using the pulse scheme in Figure S3 (see Figure 2 for additional details). Best fits to decaying single exponentials are shown as solid lines.

Table S1. Backbone amide ^{15}N longitudinal PREs, Γ_1^N, and ^{15}N-Cu^{2+} distances, $r_{N\text{-}Cu}$, derived from R_1 measurements in DCN-28EDTA-Cu^{2+} and DCN-28EDTA-Zn^{2+}.

Residue	$R_1(Cu^{2+})$ (s^{-1})	$R_1(Zn^{2+})$ (s^{-1})	Γ_1^N (s^{-1})	$r_{N\text{-}Cu}$ (Å)
Q2	0.083 ± 0.005	0.042 ± 0.004	0.041 ± 0.007	$17.8^{+0.5}_{-0.4}$
K4	0.064 ± 0.005	0.027 ± 0.007	0.037 ± 0.008	$18.1^{+0.8}_{-0.6}$
L5	0.082 ± 0.003	0.043 ± 0.009	0.039 ± 0.010	$17.9^{+0.9}_{-0.7}$
I6	0.060 ± 0.003	0.015 ± 0.007	0.045 ± 0.007	$17.5^{+0.5}_{-0.4}$
L7	0.063 ± 0.004	0.026 ± 0.007	0.037 ± 0.008	$18.1^{+0.8}_{-0.6}$
N8	0.061 ± 0.005	0.029 ± 0.004	0.032 ± 0.007	$18.6^{+0.8}_{-0.6}$
G9	0.097 ± 0.005	0.044 ± 0.004	0.053 ± 0.006	$17.0^{+0.4}_{-0.3}$
K10	0.174 ± 0.009	0.069 ± 0.006	0.106 ± 0.011	$15.2^{+0.3}_{-0.2}$
T11	0.148 ± 0.008	0.068 ± 0.005	0.080 ± 0.009	$15.9^{+0.3}_{-0.3}$
L12	0.127 ± 0.007	0.092 ± 0.006	0.035 ± 0.010	$18.3^{+1.0}_{-0.7}$
K13	0.063 ± 0.004	0.021 ± 0.005	0.042 ± 0.006	$17.7^{+0.4}_{-0.4}$
G14	0.109 ± 0.005	0.059 ± 0.005	0.049 ± 0.007	$17.3^{+0.4}_{-0.4}$
E15	0.088 ± 0.005	0.044 ± 0.005	0.044 ± 0.007	$17.6^{+0.5}_{-0.5}$
T18	0.106 ± 0.012	0.068 ± 0.010	0.038 ± 0.015	$18.0^{+1.6}_{-1.0}$
E19	0.165 ± 0.006	0.099 ± 0.008	0.067 ± 0.009	$16.4^{+0.4}_{-0.3}$
A20	0.103 ± 0.004	0.039 ± 0.003	0.063 ± 0.005	$16.6^{+0.2}_{-0.2}$
V21	0.175 ± 0.002	0.061 ± 0.006	0.114 ± 0.006	$15.0^{+0.2}_{-0.1}$
A24	0.42 ± 0.02	0.072 ± 0.005	0.35 ± 0.02	$12.5^{+0.2}_{-0.1}$
T25	0.88 ± 0.05	0.035 ± 0.005	0.84 ± 0.05	$10.8^{+0.1}_{-0.1}$
A26	0.258 ± 0.009	0.020 ± 0.008	0.238 ± 0.012	$13.3^{+0.1}_{-0.1}$
E27	0.299 ± 0.011	0.035 ± 0.002	0.264 ± 0.011	$13.0^{+0.1}_{-0.1}$
C28	0.58 ± 0.09	0.028 ± 0.008	0.55 ± 0.09	$11.5^{+0.3}_{-0.3}$
V29	0.55 ± 0.03	0.018 ± 0.005	0.53 ± 0.03	$11.6^{+0.1}_{-0.1}$
F30	0.259 ± 0.006	0.011 ± 0.006	0.248 ± 0.009	$13.2^{+0.1}_{-0.1}$
K31	0.41 ± 0.03	0.007 ± 0.007	0.40 ± 0.03	$12.1^{+0.1}_{-0.1}$
Q32	0.61 ± 0.04	0.017 ± 0.005	0.59 ± 0.04	$11.4^{+0.1}_{-0.1}$
Y33	0.213 ± 0.005	0.025 ± 0.007	0.188 ± 0.008	$13.8^{+0.1}_{-0.1}$
A34	0.152 ± 0.005	0.030 ± 0.005	0.122 ± 0.007	$14.8^{+0.1}_{-0.1}$
N35	0.209 ± 0.004	0.029 ± 0.005	0.181 ± 0.007	$13.9^{+0.1}_{-0.1}$
D36	0.153 ± 0.006	0.018 ± 0.005	0.136 ± 0.007	$14.6^{+0.1}_{-0.1}$
N37	0.115 ± 0.010	0.043 ± 0.008	0.072 ± 0.013	$16.2^{+0.5}_{-0.4}$
G38	0.128 ± 0.005	0.052 ± 0.006	0.076 ± 0.008	$16.1^{+0.3}_{-0.3}$
V39	0.159 ± 0.007	0.053 ± 0.007	0.106 ± 0.010	$15.2^{+0.3}_{-0.2}$
D40	0.329 ± 0.014	0.156 ± 0.005	0.173 ± 0.015	$14.0^{+0.2}_{-0.2}$

G41	0.53 ± 0.03	0.295 ± 0.012	0.23 ± 0.03	$13.3^{+0.3}_{-0.2}$
E42	0.210 ± 0.007	0.053 ± 0.005	0.157 ± 0.008	$14.2^{+0.1}_{-0.1}$
W43	0.223 ± 0.004	0.043 ± 0.004	0.180 ± 0.006	$13.9^{+0.1}_{-0.1}$
T44	0.116 ± 0.007	0.021 ± 0.006	0.096 ± 0.009	$15.4^{+0.3}_{-0.2}$
Y45	0.101 ± 0.004	0.015 ± 0.005	0.086 ± 0.015	$15.7^{+0.2}_{-0.2}$
D46	0.074 ± 0.004	0.029 ± 0.007	0.045 ± 0.008	$17.5^{+0.6}_{-0.5}$
D47	0.101 ± 0.003	0.044 ± 0.005	0.058 ± 0.006	$16.8^{+0.3}_{-0.3}$
A48	0.126 ± 0.006	0.065 ± 0.007	0.060 ± 0.009	$16.7^{+0.4}_{-0.4}$
T49	0.153 ± 0.007	0.107 ± 0.012	0.046 ± 0.014	$17.5^{+1.1}_{-0.7}$
K50	0.115 ± 0.005	0.059 ± 0.011	0.056 ± 0.012	$16.9^{+0.7}_{-0.5}$
T51	0.072 ± 0.004	0.028 ± 0.004	0.044 ± 0.006	$17.6^{+0.4}_{-0.4}$
F52	0.063 ± 0.005	0.009 ± 0.004	0.054 ± 0.006	$17.0^{+0.4}_{-0.3}$
T53	0.059 ± 0.005	0.018 ± 0.008	0.041 ± 0.010	$17.8^{+0.8}_{-0.6}$
T55	0.084 ± 0.003	0.008 ± 0.006	0.075 ± 0.007	$16.1^{+0.2}_{-0.2}$
E56	0.158 ± 0.008	0.051 ± 0.004	0.107 ± 0.009	$15.2^{+0.2}_{-0.2}$

Table S2. Backbone amide ^{15}N longitudinal PREs, Γ_1^N, and ^{15}N-Cu^{2+} distances, $r_{N\text{-}Cu}$, derived from R_1 measurements in CN-8EDTA-Cu^{2+} and CN-8EDTA-Zn^{2+}.

Residue	$R_1(Cu^{2+})$ (s^{-1})	$R_1(Zn^{2+})$ (s^{-1})	Γ_1^N (s^{-1})	$r_{N\text{-}Cu}$ (Å)
Q2	0.132 ± 0.007	0.040 ± 0.008	0.092 ± 0.011	$15.6^{+0.3}_{-0.3}$
K4	0.171 ± 0.012	0.028 ± 0.005	0.143 ± 0.013	$14.4^{+0.2}_{-0.2}$
L5	0.32 ± 0.02	0.057 ± 0.005	0.26 ± 0.02	$13.1^{+0.2}_{-0.2}$
G9	0.61 ± 0.04	0.269 ± 0.016	0.34 ± 0.05	$12.5^{+0.3}_{-0.3}$
G14	0.59 ± 0.05	0.070 ± 0.006	0.52 ± 0.05	$11.6^{+0.2}_{-0.2}$
E15	0.59 ± 0.11	0.051 ± 0.005	0.54 ± 0.11	$11.6^{+0.4}_{-0.3}$
T17	0.24 ± 0.04	0.144 ± 0.014	0.09 ± 0.04	$15.6^{+1.8}_{-1.0}$
T18	0.168 ± 0.013	0.076 ± 0.006	0.092 ± 0.014	$15.5^{+0.4}_{-0.4}$
E19	0.172 ± 0.007	0.087 ± 0.007	0.085 ± 0.010	$15.8^{+0.3}_{-0.3}$
A20	0.107 ± 0.015	0.048 ± 0.007	0.059 ± 0.017	$16.8^{+1.0}_{-0.7}$
V21	0.134 ± 0.012	0.041 ± 0.006	0.093 ± 0.014	$15.5^{+0.4}_{-0.4}$
A24	0.107 ± 0.005	0.046 ± 0.003	0.060 ± 0.006	$16.7^{+0.3}_{-0.3}$
T25	0.104 ± 0.011	0.016 ± 0.004	0.088 ± 0.012	$15.7^{+0.4}_{-0.3}$
A26	0.101 ± 0.007	0.026 ± 0.004	0.074 ± 0.008	$16.1^{+0.3}_{-0.3}$
E27	0.092 ± 0.013	0.028 ± 0.009	0.065 ± 0.016	$16.5^{+0.8}_{-0.6}$
K28	0.109 ± 0.006	0.030 ± 0.002	0.078 ± 0.006	$16.0^{+0.2}_{-0.2}$
V29	0.089 ± 0.010	0.011 ± 0.007	0.078 ± 0.012	$16.0^{+0.5}_{-0.4}$
F30	0.084 ± 0.007	0.009 ± 0.008	0.076 ± 0.010	$16.1^{+0.4}_{-0.3}$
K31	0.079 ± 0.009	0.016 ± 0.006	0.063 ± 0.011	$16.6^{+0.5}_{-0.4}$
Q32	0.083 ± 0.011	0.009 ± 0.007	0.074 ± 0.013	$16.1^{+0.5}_{-0.4}$
Y33	0.088 ± 0.005	0.011 ± 0.005	0.077 ± 0.007	$16.0^{+0.3}_{-0.2}$
A34	0.094 ± 0.008	0.018 ± 0.005	0.076 ± 0.009	$16.1^{+0.4}_{-0.3}$
N35	0.099 ± 0.008	0.024 ± 0.004	0.075 ± 0.009	$16.1^{+0.3}_{-0.3}$
D36	0.092 ± 0.004	0.027 ± 0.004	0.066 ± 0.006	$16.4^{+0.3}_{-0.2}$
N37	0.123 ± 0.011	0.037 ± 0.005	0.087 ± 0.012	$15.7^{+0.4}_{-0.3}$
G38	0.119 ± 0.005	0.051 ± 0.004	0.068 ± 0.006	$16.4^{+0.3}_{-0.2}$
V39	0.198 ± 0.007	0.050 ± 0.004	0.148 ± 0.008	$14.4^{+0.1}_{-0.1}$
D40	0.38 ± 0.02	0.146 ± 0.013	0.24 ± 0.03	$13.3^{+0.3}_{-0.2}$
G41	0.181 ± 0.017	0.05 ± 0.02	0.13 ± 0.03	$14.6^{+0.5}_{-0.4}$
W43	0.315 ± 0.019	0.049 ± 0.007	0.27 ± 0.02	$13.0^{+0.2}_{-0.2}$
T44	0.24 ± 0.02	0.014 ± 0.013	0.22 ± 0.03	$13.4^{+0.3}_{-0.2}$
Y45	0.158 ± 0.010	0.016 ± 0.009	0.142 ± 0.014	$14.5^{+0.2}_{-0.2}$
D46	0.171 ± 0.011	0.028 ± 0.004	0.143 ± 0.012	$14.4^{+0.2}_{-0.2}$
D47	0.149 ± 0.010	0.036 ± 0.004	0.113 ± 0.011	$15.0^{+0.3}_{-0.2}$

A48	0.133 ± 0.015	0.059 ± 0.004	0.075 ± 0.016	$16.1^{+0.6}_{-0.5}$
T49	0.211 ± 0.008	0.121 ± 0.010	0.090 ± 0.013	$15.6^{+0.4}_{-0.3}$
K50	0.17 ± 0.02	0.056 ± 0.014	0.11 ± 0.02	$15.1^{+0.6}_{-0.5}$
T51	0.155 ± 0.010	0.020 ± 0.005	0.135 ± 0.011	$14.6^{+0.2}_{-0.2}$
F52	0.197 ± 0.013	0.015 ± 0.003	0.182 ± 0.013	$13.9^{+0.2}_{-0.2}$
T53	0.316 ± 0.018	0.022 ± 0.009	0.29 ± 0.02	$12.8^{+0.2}_{-0.1}$
T55	0.57 ± 0.11	0.029 ± 0.010	0.54 ± 0.11	$11.6^{+0.4}_{-0.4}$
E56	0.24 ± 0.05	0.040 ± 0.005	0.20 ± 0.05	$13.6^{+0.6}_{-0.5}$

Table S3. Comparison of experimental ^{15}N longitudinal PREs and ^{15}N-Cu^{2+} distances with corresponding values derived from a structural model of 28EDTA-Cu^{2+}.

Residue	Γ_1^N from Experiment (s^{-1})	Γ_1^N from Structure (s^{-1})	$r_{N\text{-}Cu}$ from Experiment (Å)	$r_{N\text{-}Cu}$ from Structure (Å)
Q2	0.041 ± 0.007	0.015	$17.8^{+0.5}_{-0.4}$	21.0
K4	0.037 ± 0.008	0.013	$18.1^{+0.8}_{-0.6}$	21.5
L5	0.039 ± 0.010	0.012	$17.9^{+0.9}_{-0.7}$	21.8
I6	0.045 ± 0.007	0.008	$17.5^{+0.5}_{-0.4}$	23.6
L7	0.037 ± 0.008	0.005	$18.1^{+0.8}_{-0.6}$	25.0
N8	0.032 ± 0.007	0.004	$18.6^{+0.8}_{-0.6}$	26.5
G9	0.053 ± 0.006	0.003	$17.0^{+0.4}_{-0.3}$	27.2
K10	0.106 ± 0.011	0.002	$15.2^{+0.3}_{-0.2}$	28.8
T11	0.080 ± 0.009	0.002	$15.9^{+0.3}_{-0.3}$	29.7
L12	0.035 ± 0.010	0.003	$18.3^{+1.0}_{-0.7}$	28.4
K13	0.042 ± 0.006	0.002	$17.7^{+0.4}_{-0.4}$	28.6
G14	0.049 ± 0.007	0.003	$17.3^{+0.4}_{-0.4}$	28.2
E15	0.044 ± 0.007	0.003	$17.6^{+0.5}_{-0.5}$	26.9
T18	0.038 ± 0.015	0.023	$18.0^{+1.6}_{-1.0}$	19.6
E19	0.067 ± 0.009	0.039	$16.4^{+0.4}_{-0.3}$	18.0
A20	0.063 ± 0.005	0.074	$16.6^{+0.2}_{-0.2}$	16.1
V21	0.114 ± 0.006	0.155	$15.0^{+0.2}_{-0.1}$	14.3
A24	0.35 ± 0.02	0.275	$12.5^{+0.2}_{-0.1}$	13.0
T25	0.84 ± 0.05	0.773	$10.8^{+0.1}_{-0.1}$	10.9
A26	0.238 ± 0.012	0.340	$13.3^{+0.1}_{-0.1}$	12.5
E27	0.264 ± 0.011	0.253	$13.0^{+0.1}_{-0.1}$	13.1
C28	0.55 ± 0.09	0.726	$11.5^{+0.3}_{-0.3}$	11.0
V29	0.53 ± 0.03	0.613	$11.6^{+0.1}_{-0.1}$	11.3
F30	0.248 ± 0.009	0.169	$13.2^{+0.1}_{-0.1}$	14.1
K31	0.40 ± 0.03	0.157	$12.1^{+0.1}_{-0.1}$	14.2
Q32	0.59 ± 0.04	0.235	$11.4^{+0.1}_{-0.1}$	13.3
Y33	0.188 ± 0.008	0.096	$13.8^{+0.1}_{-0.1}$	15.4
A34	0.122 ± 0.007	0.043	$14.8^{+0.1}_{-0.1}$	17.6
N35	0.181 ± 0.007	0.046	$13.9^{+0.1}_{-0.1}$	17.5
D36	0.136 ± 0.007	0.041	$14.6^{+0.1}_{-0.1}$	17.8
N37	0.072 ± 0.013	0.019	$16.2^{+0.5}_{-0.4}$	20.3
G38	0.076 ± 0.008	0.012	$16.1^{+0.3}_{-0.3}$	21.8
V39	0.106 ± 0.010	0.012	$15.2^{+0.3}_{-0.2}$	22.0

D40	0.173 ± 0.015	0.012	$14.0^{+0.2}_{-0.2}$	21.9
G41	0.23 ± 0.03	0.013	$13.3^{+0.3}_{-0.2}$	21.6
E42	0.157 ± 0.008	0.009	$14.2^{+0.1}_{-0.1}$	22.8
W43	0.180 ± 0.006	0.014	$13.9^{+0.1}_{-0.1}$	21.3
T44	0.096 ± 0.009	0.013	$15.4^{+0.3}_{-0.2}$	21.6
Y45	0.086 ± 0.015	0.015	$15.7^{+0.2}_{-0.2}$	21.2
D46	0.045 ± 0.008	0.010	$17.5^{+0.6}_{-0.5}$	22.6
D47	0.058 ± 0.006	0.009	$16.8^{+0.3}_{-0.3}$	23.1
A48	0.060 ± 0.009	0.005	$16.7^{+0.4}_{-0.4}$	25.3
T49	0.046 ± 0.014	0.004	$17.5^{+1.1}_{-0.7}$	26.0
K50	0.056 ± 0.012	0.007	$16.9^{+0.7}_{-0.5}$	23.8
T51	0.044 ± 0.006	0.010	$17.6^{+0.4}_{-0.4}$	22.7
F52	0.054 ± 0.006	0.014	$17.0^{+0.4}_{-0.3}$	21.4
T53	0.041 ± 0.010	0.011	$17.8^{+0.8}_{-0.6}$	22.1
T55	0.075 ± 0.007	0.007	$16.1^{+0.2}_{-0.2}$	24.2
E56	0.107 ± 0.009	0.004	$15.2^{+0.2}_{-0.2}$	26.5

Table S4. Comparison of experimental ^{15}N longitudinal PREs and ^{15}N-Cu^{2+} distances with corresponding values derived from a structural model of 8EDTA-Cu^{2+}.

Residue	Γ_1^N from Experiment (s^{-1})	Γ_1^N from Structure (s^{-1})	$r_{N\text{-}Cu}$ from Experiment (Å)	$r_{N\text{-}Cu}$ from Structure (Å)
Q2	0.092 ± 0.011	0.011	$15.6^{+0.3}_{-0.3}$	22.2
K4	0.143 ± 0.013	0.081	$14.4^{+0.2}_{-0.2}$	15.9
L5	0.26 ± 0.02	0.169	$13.1^{+0.2}_{-0.2}$	14.1
G9	0.34 ± 0.05	0.400	$12.5^{+0.3}_{-0.3}$	12.2
G14	0.52 ± 0.05	0.612	$11.6^{+0.2}_{-0.2}$	11.3
E15	0.54 ± 0.11	0.372	$11.6^{+0.4}_{-0.3}$	12.3
T17	0.09 ± 0.04	0.046	$15.6^{+1.8}_{-1.0}$	17.5
T18	0.092 ± 0.014	0.022	$15.5^{+0.4}_{-0.4}$	19.8
E19	0.085 ± 0.010	0.009	$15.8^{+0.3}_{-0.3}$	23.0
A20	0.059 ± 0.017	0.006	$16.8^{+1.0}_{-0.7}$	24.4
V21	0.093 ± 0.014	0.004	$15.5^{+0.4}_{-0.4}$	26.8
A24	0.060 ± 0.006	0.007	$16.7^{+0.3}_{-0.3}$	23.7
T25	0.088 ± 0.012	0.005	$15.7^{+0.4}_{-0.3}$	24.9
A26	0.074 ± 0.008	0.009	$16.1^{+0.3}_{-0.3}$	23.1
E27	0.065 ± 0.016	0.014	$16.5^{+0.8}_{-0.6}$	21.3
K28	0.078 ± 0.006	0.009	$16.0^{+0.2}_{-0.2}$	22.9
V29	0.078 ± 0.012	0.008	$16.0^{+0.5}_{-0.4}$	23.4
F30	0.076 ± 0.010	0.016	$16.1^{+0.4}_{-0.3}$	20.9
K31	0.063 ± 0.011	0.018	$16.6^{+0.5}_{-0.4}$	20.4
Q32	0.074 ± 0.013	0.010	$16.1^{+0.5}_{-0.4}$	22.6
Y33	0.077 ± 0.007	0.012	$16.0^{+0.3}_{-0.2}$	21.9
A34	0.076 ± 0.009	0.021	$16.1^{+0.4}_{-0.3}$	19.8
N35	0.075 ± 0.009	0.014	$16.1^{+0.3}_{-0.3}$	21.3
D36	0.066 ± 0.006	0.008	$16.4^{+0.3}_{-0.2}$	23.4
N37	0.087 ± 0.012	0.011	$15.7^{+0.4}_{-0.3}$	22.2
G38	0.068 ± 0.006	0.012	$16.4^{+0.3}_{-0.2}$	21.8
V39	0.148 ± 0.008	0.022	$14.4^{+0.1}_{-0.1}$	19.8
D40	0.24 ± 0.03	0.029	$13.3^{+0.3}_{-0.2}$	18.8
G41	0.13 ± 0.03	0.044	$14.6^{+0.5}_{-0.4}$	17.6
W43	0.27 ± 0.02	0.112	$13.0^{+0.2}_{-0.2}$	15.1
T44	0.22 ± 0.03	0.213	$13.4^{+0.3}_{-0.2}$	13.5
Y45	0.142 ± 0.014	0.143	$14.5^{+0.2}_{-0.2}$	14.5
D46	0.143 ± 0.012	0.160	$14.4^{+0.2}_{-0.2}$	14.2

D47	0.113 ± 0.011	0.066	$15.0^{+0.3}_{-0.2}$	16.4
A48	0.075 ± 0.016	0.064	$16.1^{+0.6}_{-0.5}$	16.5
T49	0.090 ± 0.013	0.115	$15.6^{+0.4}_{-0.3}$	15.0
K50	0.11 ± 0.02	0.086	$15.1^{+0.6}_{-0.5}$	15.7
T51	0.135 ± 0.011	0.157	$14.6^{+0.2}_{-0.2}$	14.2
F52	0.182 ± 0.013	0.228	$13.9^{+0.2}_{-0.2}$	13.4
T53	0.29 ± 0.02	0.479	$12.8^{+0.2}_{-0.1}$	11.8
T55	0.54 ± 0.11	0.416	$11.6^{+0.4}_{-0.4}$	12.1
E56	0.20 ± 0.05	0.269	$13.6^{+0.6}_{-0.5}$	13.0

References

(1) Nadaud, P. S.; Helmus, J. J.; Hofer, N.; Jaroniec, C. P. *J. Am. Chem. Soc.* **2007,** 129, 7502-7503.

(2) Ermácora, M. R.; Delfino, J. M.; Cuenoud, B.; Schepartz, A.; Fox, R. O. *Proc. Natl. Acad. Sci. USA* **1992,** 89, 6383-6387; Ebright, Y. W.; Chen, Y.; Pendergrast, S.; Ebright, R. H. *Biochemistry* **1992,** 31, 10664-10670.

(3) Nadaud, P. S.; Helmus, J. J.; Kall, S. L.; Jaroniec, C. P. *J. Am. Chem. Soc.* **2009,** 131, 8108-8120.

(4) Delaglio, F.; Grzesiek, S.; Vuister, G. W.; Zhu, G.; Pfeifer, J.; Bax, A. *J. Biomol. NMR* **1995,** 6, 277-293.

(5) Goddard, T. D.; Kneller, D. G. **1993**, SPARKY 3, University of California, San Francisco.

(6) Pines, A.; Gibby, M. G.; Waugh, J. S. *J. Chem. Phys.* **1973,** 59, 569-590.

(7) Hediger, S.; Meier, B. H.; Ernst, R. R. *Chem. Phys. Lett.* **1995,** 240, 449-456.

(8) Detken, A.; Hardy, E. H.; Ernst, M.; Meier, B. H. *Chem. Phys. Lett.* **2002,** 356, 298-304.

(9) Shaka, A. J.; Keeler, J.; Freeman, R. *J. Mag. Reson.* **1983,** 53, 313-340.

(10) Baldus, M.; Petkova, A. T.; Herzfeld, J.; Griffin, R. G. *Mol. Phys.* **1998,** 95, 1197-1207.

(11) Laage, S.; Lesage, A.; Emsley, L.; Bertini, I.; Felli, I. C.; Pierattelli, R.; Pintacuda, G. *J. Am. Chem. Soc.* **2009,** 131, 10816-10817.

(12) Kupce, E.; Boyd, J.; Campbell, I. D. *J. Magn. Reson. B* **1995,** 106, 300-303.

(13) States, D. J.; Haberkorn, R. A.; Ruben, D. J. *J. Magn. Reson.* **1982,** 48, 286-292.

(14) Verel, R.; Baldus, M.; Ernst, M.; Meier, B. H. *Chem. Phys. Lett.* **1998,** 287, 421-428.

(15) Giraud, N.; Bockmann, A.; Lesage, A.; Penin, F.; Blackledge, M.; Emsley, L. *J. Am. Chem. Soc.* **2004,** 126, 11422-11423.